Smart Structures and Systems, *Vol. 26, No. 3 (2020) 373-390*
DOI: https://doi.org/10.12989/sss.2020.26.3.373

Performance validation and application of a mixed force-displacement loading strategy for bi-directional hybrid simulation

Zhen Wang [1,2a], Qiyang Tan [2], Pengfei Shi [3,4], Ge Yang*[1],
Siyu Zhu [2], Guoshan Xu [2], Bin Wu [1,2] and Jianyun Sun [4]

[1] *School of Civil Engineering and Architecture, Wuhan University of Technology, Wuhan 430070, China*
[2] *School of Civil Engineering, Harbin Institute of Technology, Harbin 150090, China*
[3] *China Construction Science & Technology Corporation Limited, Beijing 100195, China*
[4] *China State Construction Engineering Corporation Limited, Technical Center, Beijing 101300, China*

(*Received February 3, 2020, Revised June 3, 2020, Accepted June 8, 2020*)

Abstract. Hybrid simulation (HS) is a versatile tool for structural performance evaluation under dynamic loads. Although real structural responses are often multiple-directional owing to an eccentric mass/stiffness of the structure and/or excitations not along structural major axes, few HS in this field takes into account structural responses in multiple directions. Multi-directional loading is more challenging than uni-directional loading as there is a nonlinear transformation between actuator and specimen coordinate systems, increasing the difficulty of suppressing loading error. Moreover, redundant actuators may exist in multi-directional hybrid simulations of large-scale structures, which requires the loading strategy to contain ineffective loading of multiple actuators. To address these issues, lately a new strategy was conceived for accurate reproduction of desired displacements in bi-directional hybrid simulations (BHS), which is characterized in two features, i.e., iterative displacement command updating based on the Jacobian matrix considering nonlinear geometric relationships, and force-based control for compensating ineffective forces of redundant actuators. This paper performs performance validation and application of this new mixed loading strategy. In particular, virtual BHS considering linear and nonlinear specimen models, and the diversity of actuator properties were carried out. A validation test was implemented with a steel frame specimen. A real application of this strategy to BHS on a full-scale 2-story frame specimen was performed. Studies showed that this strategy exhibited excellent tracking performance for the measured displacements of the control point and remarkable compensation for ineffective forces of the redundant actuator. This strategy was demonstrated to be capable of accurately and effectively reproducing the desired displacements in large-scale BHS.

Keywords: bi-directional hybrid simulation; bi-directional pseudo-dynamic test; mixed force-displacement loading; redundant actuator; force distribution optimization

1. Introduction

In the past three decades, hybrid simulations were widely investigated and extensively applied for performance evaluation of structures subjected to dynamic loads, e.g., an earthquake (Nakashima *et al*. 1992, Wu *et al*. 2007, Chae *et al*. 2014, Wang *et al*. 2016, Shao *et al*. 2016, Liu *et al*. 2020) and wind (Wu and Song 2019). This method is attractive and promising for its unique advantages over other alternatives, such as quasi-static testing and shaking table testing (Pan *et al*. 2015). This method separates emulated structures into two portions, namely numerical substructures (NS) and physical substructures (PS) (Nakashima *et al*. 1985). The NS are computationally modeled in that their behavior has been fairly well understood. Conversely, the PS are physically fabricated and experimented in laboratories since they are so complicated to be numerically simulated. This technique takes advantage of numerical simulations and physical experiments and achieves versatile performance in terms of low cost on specimens and setups, accurate testing results and so on.

One critical issue associated with this method is the accurate reproduction of the boundary condition. Numerous efforts have been paid and a great variety of strategies are available, including displacement-based control methods (Wagg and Stoten 2001, Ou *et al*. 2015, Phillips *et al*. 2014), force-based control methods (Nakata *et al*. 2014, Zhao *et al*. 2014, Wang *et al*. 2018), mixed force-displacement control methods (Pan *et al*. 2014), and delay compensation methods (Horiuchi *et al*. 1999, Ahmadizadeh *et al*. 2008, Wu *et al*. 2013, Wang *et al*. 2014, 2019a, Tang *et al*. 2018). However, although real structures generate responses in multiple directions owing to an eccentric mass/stiffness of the structure and/or excitations which are not along structural major axes, these studies are often carried out for problems in one direction. In uni-directional hybrid simulations, the seismic damage is often underestimated as the ignored torsional deformation aggravates the structural deformation and leads to the buckling and/or even collapse of structures, while bi-directional hybrid simulations can more realistically

*Corresponding author, Ph.D., Assistant Professor,
E-mail: yangge@whut.edu.cn
[a] Ph.D., Assistant Professor, E-mail: zhenwang@hit.edu.cn

http://www.techno-press.org/?journal=sss&subpage=7
ISSN: 1738-1584 (Print), 1738-1991 (Online)

reproduce the multiple directional responses of the structure. In this sense, bi-directional hybrid simulation is a better choice to realistically investigate the seismic performance of structures (Takanashi *et al*. 1980, Iqbal *et al*. 2008, Khoo *et al*. 2016).

Several studies were performed and successfully made great progress in testing techniques of bi-directional hybrid simulations (BHS). Thewalt and Mahin (1995) carried out the first bi-directional pseudo-dynamic test (PDT) using a linear transformation from the displacements of the control point (CP) to actuator elongations. Molina *et al*. (1999) performed the first large-scale bi-directional PDT on a full-size three-story building subjected to strong earthquake motion. This test considered a nonlinear transformation between actuator and specimen coordinate systems. Generalized displacements of the CP were controlled by feeding back the readings of external displacement transducers mounted on sliders. The redundant actuator was operated using its internal displacement in conjunction with command correction based on a discrepancy between optimal and actual forces. Liu and Chang (2000) proposed a bi-axial pseudo-dynamic technique for testing structures under two lateral perpendicular seismic excitations, which accounts for the analytical geometrical relationships among the rigid specimen, the actuators and the reaction frames. The specimen displacement was determined using four actuator displacements by minimizing a cost function. Satisfactory results were obtained in the bi-axial PDT with a mass-eccentric and stiffness-symmetric specimen. However, drifts of the CP response were observed in tests. PDT substructuring testing considering two in-plane orthogonal translations and one in-plane rotation was adopted to investigate seismic performance of steel frames with hybrid steel shear panels by Tsai *et al*. (2001). This study employed three actuators connected to a transfer girder to impose the command displacements. To enforce the constant vertical load representing the gravity, a mixed displacement-force correction technique was conceived and implemented. In order to correct kinematic errors in planar multi-directional PDT, Mercan *et al*. (2009) presented two transformation methods, namely incremental and total kinematic transformation methods. The former employed linear displacement transformations, while the latter was formulated based on accurate nonlinear displacement transformations and enabled the specimen displacement to be solved without iteration. These methods required less computational time and hence, were suitable for fast and even real-time PDT. However, the second method required connecting two displacement transducers to the same specimen node, which might limit the application of this method. Fermandois and Spencer (2017) adopted the incremental kinematic transformation method for fast computation in real-time hybrid simulations, in which a small sampling time step was used to ensure accuracy. Chang *et al*. (2015) proposed a high-precision positioning correction method for hybrid simulation using multiple degree-of-freedom (DOF) loading units for accommodating the elastic deformation at the reaction wall and/or connections. The proposed online correction method adjusted the displacement commands using the difference between the desired and achieved displacements using an iterative process. This correction process can successfully suppress loading error; however, the nonlinear transformation from the CP displacements to actuator commands were not clearly deployed to this correction. To achieve desirable tracking performance, a more accurate transformation is needed. Despite the nonlinearity of transformation, errors in actuator configuration (e.g., pin location, actuator length, etc.) also influence the coordinator transformation. Nakata *et al.* (2010) presented a sensitivity-based method to consider the transformation error caused by inaccurate initial actuator length data. As such errors can not be eliminated based on internal measurements of actuators, external measurement devices were used in his study.

This literature review shows that (1) displacement command updating according to loading errors is essential for accurate and reliable testing results in BHS. Multi-directional loading is more challenging for its diversity of actuator properties in one test. To be specific, actuators available for one BHS often possess different loading rates, loading capacities, and/or different dimensions. As a consequence, displacement correction must be effectively implemented to suppress error accumulation and propagation (Liu and Chang 2000); (2) more actuators than the DOF number of the CP displacements are often required owing to insufficient loading capacities of actuators. This indicates that loading strategies of redundant actuators must be carefully treated; (3) validation and application tests on large-scale specimens have to be implemented to realistically reflect the performance of testing methods. With these challenges in mind, a novel mixed force-displacement loading strategy (referred to as the new loading strategy) for BHS was conceived (Wang *et al*. 2019b). This method is characterized in two features, i.e., displacement command updating based on numerical iteration considering nonlinear geometric relationships, and force-based control for redundant actuators.

This study is devoted to performance validation and application of this new loading strategy. The remaining parts of this paper are organized as follows. Section 2 presents an overview of this new strategy for BHS. Section 3 describes virtual tests with this method, considering linear and nonlinear specimen models. Subsequently, a validation test is explained in Section 4, while a real application of this strategy to a full-scale 2-story specimen is demonstrated in Section 5. Section 6 presents conclusions drawn from this study.

2. Overview of the new mixed loading strategy for BHS

The objective of loading strategies for BHS is to accurately realize desired displacements for the CP, and to optimize the load distribution among actuators in the sense of the performance index. Since the mass center of the floor is chosen as the CP herein, the desired CP displacements are computational displacements in BHS with the initial CP location as the origin point. The challenges arise owing to

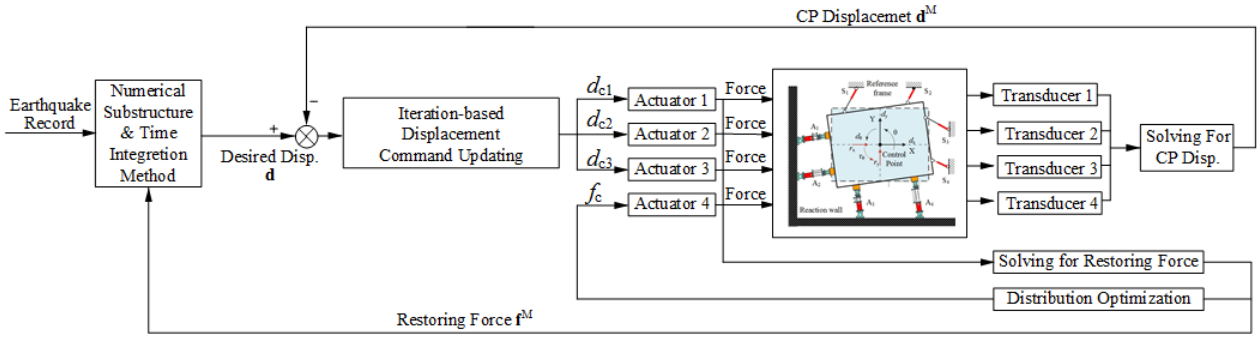

Fig. 1 BHS with the new loading strategy

Table 1 Variables in Section 2

Variable	Description
$\boldsymbol{d} = [d_x\ d_y\ d_\theta]^T$	Desired displacement vector (X-translation, Y-translation and rotation) of control point
$\boldsymbol{d}^M$	Measured displacement vector of control point
$\boldsymbol{d}^C = [d_{c1}\ d_{c2}\ d_{c3}]^T$	Displacement command vector of three displacement-controlled actuators
$\boldsymbol{d}^A$	Displacement reading vector of three displacement controlled actuators
$\boldsymbol{d}_{\mathrm{LVDT}}^M = [d_{\mathrm{LVDT}}^1\ \ d_{\mathrm{LVDT}}^2\ \ \cdots\ \ d_{\mathrm{LVDT}}^p]^T$	Reading vector of the displacement transducers
f_c	Force command of the force-controlled redundant actuator
f^i	Force reading of the *i*-th actuator
f_x^i	Projection of f^i in X-direction
f_y^i	Projection of f^i in Y-direction
M_i	Moment induced by f^i about the control point
$\boldsymbol{E}_a^i$	A unit vector in the direction of the *i*-th actuator force
$\boldsymbol{F}_L = [f_L^1\ \ f_L^2\ \ \cdots\ \ f_L^n]^T$	Optimal force vector of the actuators
f_L^i	Optimal force of the *i*-th actuator
f_m^i	Loading capacity of the i-th actuator
$\boldsymbol{r}$	Restoring force vector of control point

the diversity of the actuator characteristics and layout, strong geometric nonlinearities between the CP displacement and the actuator/transducer displacement, and material nonlinearities of the specimen. With these in mind, a new mixed loading strategy was conceived (Wang *et al*. 2019b), as shown in Fig. 1. Apparently, this method updates commands of actuators in displacement control mode using desired and actual displacements of the CP. The redundant actuator, i.e., Actuator 4, is manipulated in force mode to track its optimal force. The CP displacements are solved from readings of four displacement transducers using iteration schemes. The resultant forces of four actuators are fed back to the numerical integration scheme for evaluating the desired displacements of the next step. This section elaborates on all the components of this new strategy. For the convenience of readers, most variables employed in this section are collected and described in Table 1.

2.1 Nonlinear geometric relationships

In a BHS, both displacements of actuators and transducers are nonlinear functions of the translation and rotation of the specimen CP. The updating of actuator commands, the solving for the CP displacements, and the solving for the restoring forces, depend on these nonlinear relationships. Therefore, the correct establishment of the nonlinear relationship is crucial for performing the test.

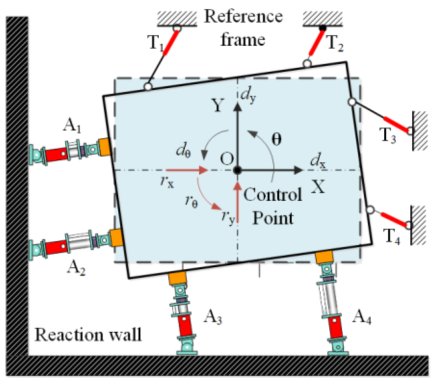

Fig. 2 Convention for the new loading strategy

For a convenient and accurate description, a coordinate system XOY is defined, which is located at the initial position of the CP, with coordinate axes (X, Y) along the positive directions of translational displacements, and the rotation (θ) in anti-clockwise. The specimen displacements consist of the translation d_x in the X direction, the translation d_y in the Y direction, and the in-plane rotation d_θ about the CP, as shown in Fig. 2. In the figure, A_1, A_2, A_3, and A_4 represent four actuators; T_1, T_2, T_3, and T_4 denote four displacement transducers; r_x, r_y, and r_θ stand for the components of the generalized restoring forces. Additionally, the specimen floor (or the transfer body for loading) is assumed rigid. Note that each actuator possesses its load cell and displacement transducer which are used for inner loop control of the actuator if necessary. This configuration is chosen as a representative for describing the method, and theoretically, this method can be applied to different setup configurations.

The initial coordinates of the movable end of the i-th actuator connected to the specimen are defined as $\boldsymbol{A}_{\mathrm{aM}}^{i,0}=[X_{\mathrm{aM}}^{i,0}\quad Y_{\mathrm{aM}}^{i,0}]^T$, and those of the fixed end of the i-th actuator connected to a reaction wall are written as $\boldsymbol{A}_{\boldsymbol{aF}}^{i,0}=[X_{\mathrm{aF}}^{i,0}\quad Y_{\mathrm{aF}}^{i,0}]^T$. The subscripts a, M and F denote actuator, movable end, and fixed end, respectively, while the upper script T stands for transpose. The initial length of the actuator is determined by means of $|\boldsymbol{A}_{\boldsymbol{aM}}^{\boldsymbol{i},\boldsymbol{0}}-\boldsymbol{A}_{\boldsymbol{aF}}^{i,0}|$, where $|\bullet|$ denotes the magnitude of a vector.

The following presents a derivation of the actuator displacement d_a^i when the CP is displaced by $\boldsymbol{d}^M$. This displacement $\boldsymbol{d}^M$ is decomposed into two parts, namely the translational displacement $\boldsymbol{d}_1^M=[d_x^M\quad d_y^M]^T$ and the rotational displacement d_θ^M. According to the rigid-body assumption, the coordinates of the movable end of the actuator can be expressed by

$$\begin{aligned} X_{\mathrm{aM}}^i &= X_{\mathrm{aM}}^{i,0}\cos d_\theta^M - Y_{\mathrm{aM}}^{i,0}\sin d_\theta^M + d_x^M \\ Y_{\mathrm{aM}}^i &= Y_{\mathrm{aM}}^{i,0}\cos d_\theta^M + X_{\mathrm{aM}}^{i,0}\sin d_\theta^M + d_y^M \end{aligned} \tag{1}$$

Rearrangement of the above expression yield

$$\boldsymbol{A}_{\mathrm{aM}}^i=\boldsymbol{T}\cdot\boldsymbol{A}_{\mathrm{aM}}^{i,0}+\boldsymbol{d}_1^M \tag{2}$$

where

$$\boldsymbol{T}=\begin{bmatrix}\cos d_\theta^M & -\sin d_\theta^M\\ \sin d_\theta^M & \cos d_\theta^M\end{bmatrix} \tag{3}$$

The change in actuator length is equal to the reading d_a^i of the actuator displacement, which can be expressed by

$$d_a^i=|\boldsymbol{A}_{\mathrm{aM}}^i-\boldsymbol{A}_{\mathrm{aF}}^{i,0}|-|\boldsymbol{A}_{\boldsymbol{aM}}^{\boldsymbol{i},\boldsymbol{0}}-\boldsymbol{A}_{\mathrm{aF}}^{i,0}| \tag{4}$$

This expression indicates the theoretical reading of the i-th actuator when the CP displacement of the specimen is $\boldsymbol{d}^M$. However, the actual reading tends to be slightly different due to gaps, bearing slips, and elastic deformation of the connector between the actuator and the specimen. Notably, Eq. (4) is more concise than those in Molina *et al.* (1999) and Liu and Chang (2000), which benefits from the definition of this coordinate system.

The nonlinear relationship between the reading of a displacement transducer and the specimen displacement can be processed similarly and will not be elaborated on here.

2.2 Specimen restoring forces

In a BHS, actuators always provide loads along their axes, i.e., axial forces; hence, the restoring forces of the specimen have to be solved according to all actual actuator forces, as shown in Fig. 1. Given the position of an actuator, one can obtain the current direction of the actuator force and force components along the coordinate axes. The resultant forces of all the actuators are equal to the restoring forces of the specimen. The following describes how to obtain these restoring forces. Dividing the actuator position vector by its magnitude gives a unit vector in the direction of the actuator force, namely

$$\boldsymbol{E}_a^i=\left(\boldsymbol{A}_{\mathrm{aM}}^i-\boldsymbol{A}_{\mathrm{aF}}^{i,0}\right)/\left|\boldsymbol{A}_{\mathrm{aM}}^i-\boldsymbol{A}_{\mathrm{aF}}^{i,0}\right| \tag{5}$$

where the actuator position vector is $\boldsymbol{A}_{\mathrm{aM}}^i-\boldsymbol{A}_{\mathrm{aF}}^{i,0}$. Hence, components of the actual force f^i of the i-th actuator are written as

$$[f_x^i\quad f_y^i]^T=f^i\cdot\boldsymbol{E}_a^i \tag{6}$$

Each force component generates a moment about the CP to balance the torque of the rotated specimen. The moment induced by the actuator force about the CP can be recast as

$$M_i=f_x^i\cdot\left(Y_{\mathrm{aM}}^i-d_y^M\right)-f_y^i\cdot\left(X_{\mathrm{aM}}^i-d_x^M\right) \tag{7}$$

The positive direction of the moment is anti-clockwise, as shown in Fig. 2. It is worth mentioning that $[d_x^M\quad d_y^M]^T$ defines the new location of the CP after the deformation. The restoring forces of the specimen equal the resultant forces of all the actuators, and hence, they are expressed as

$$\boldsymbol{r}=\boldsymbol{A}\cdot\boldsymbol{F} \tag{8}$$

where $\boldsymbol{F}$ represents a vector consisting of all actual forces of the n actuators, namely

$$\boldsymbol{F}=[f^1\quad f^2\ldots\quad f^n]^T \tag{9}$$

A is a transformation matrix from the actuator forces to the specimen restoring forces with a size of 3 × n, written as

$$\boldsymbol{A}=\begin{bmatrix}\dfrac{X_{\mathrm{aM}}^1-X_{\mathrm{aF}}^{1,0}}{\left|\boldsymbol{A}_{\mathrm{aM}}^1-\boldsymbol{A}_{\mathrm{aF}}^{1,0}\right|} & \dfrac{Y_{\mathrm{aM}}^1-Y_{\mathrm{aF}}^{1,0}}{\left|\boldsymbol{A}_{\mathrm{aM}}^1-\boldsymbol{A}_{\mathrm{aF}}^{1,0}\right|} & \dfrac{(X_{\mathrm{aM}}^1-X_{\mathrm{aF}}^{1,0})\cdot\left(Y_{\mathrm{aM}}^1-d_y^M\right)-(Y_{\mathrm{aM}}^1-Y_{\mathrm{aF}}^{1,0})\cdot(X_{\mathrm{aM}}^1-d_x^M)}{\left|\boldsymbol{A}_{\mathrm{aM}}^1-\boldsymbol{A}_{\mathrm{aF}}^{1,0}\right|}\\ \dfrac{X_{\mathrm{aM}}^2-X_{\mathrm{aF}}^{2,0}}{\left|\boldsymbol{A}_{\mathrm{aM}}^2-\boldsymbol{A}_{\mathrm{aF}}^{2,0}\right|} & \dfrac{Y_{\mathrm{aM}}^2-Y_{\mathrm{aF}}^{2,0}}{\left|\boldsymbol{A}_{\mathrm{aM}}^2-\boldsymbol{A}_{\mathrm{aF}}^{2,0}\right|} & \dfrac{(X_{\mathrm{aM}}^2-X_{\mathrm{aF}}^{2,0})\cdot\left(Y_{\mathrm{aM}}^2-d_y^M\right)-(Y_{\mathrm{aM}}^2-Y_{\mathrm{aF}}^{2,0})\cdot(X_{\mathrm{aM}}^2-d_x^M)}{\left|\boldsymbol{A}_{\mathrm{aM}}^2-\boldsymbol{A}_{\mathrm{aF}}^{2,0}\right|}\\ \cdots & \cdots & \cdots\\ \dfrac{X_{\mathrm{aM}}^n-X_{\mathrm{aF}}^{n,0}}{\left|\boldsymbol{A}_{\mathrm{aM}}^n-\boldsymbol{A}_{\mathrm{aF}}^{n,0}\right|} & \dfrac{Y_{\mathrm{aM}}^n-Y_{\mathrm{aF}}^{n,0}}{\left|\boldsymbol{A}_{\mathrm{aM}}^n-\boldsymbol{A}_{\mathrm{aF}}^{n,0}\right|} & \dfrac{(X_{\mathrm{aM}}^n-X_{\mathrm{aF}}^{n,0})\cdot\left(Y_{\mathrm{aM}}^n-d_y^M\right)-(Y_{\mathrm{aM}}^n-Y_{\mathrm{aF}}^{n,0})\cdot(X_{\mathrm{aM}}^n-d_x^M)}{\left|\boldsymbol{A}_{\mathrm{aM}}^n-\boldsymbol{A}_{\mathrm{aF}}^{n,0}\right|}\end{bmatrix}^T \tag{10}$$

2.3 Control point displacements

In a real BHS, actuator displacements are not accurate enough to determine the CP displacement owing to specimen slip and connector deformation (Xu *et al*. 2017). To improve the test accuracy, the CP displacement is solved based on the nonlinear geometric relationship and the readings of additional displacement transducers. This solution is incorporated into the new displacement loading strategy to achieve high-precision reproduction of the boundary condition for BHS.

Differently from those in Molina *et al*. (1999), displacement transducers herein are installed with two spherical hinge bearings, referring to Fig. 20(c). This indicates that the nonlinear transformation relationship between the transducer reading $\boldsymbol{d}_{\mathrm{LVDT}}^{M}$ and the CP displacement $\boldsymbol{d^M}$ is consistent with that described in Section 2.1. Analogous to Eq. (4), the reading of the *i*-th transducer is a function of $\boldsymbol{d^M}$, that is

$$d_{\mathrm{LVDT}}^{i} = |\boldsymbol{M}_{\mathrm{aM}}^{i} - \boldsymbol{M}_{\mathrm{aF}}^{i,0}| - |\boldsymbol{M}_{\mathrm{aM}}^{i,0} - \boldsymbol{M}_{\mathrm{aF}}^{i,0}| \tag{11}$$

where $\boldsymbol{M}_{\mathrm{aM}}^{i}$ and $\boldsymbol{M}_{\mathrm{aF}}^{i,0}$ denote the coordinates of the movable and fixed ends of the transducer, respectively. Similarly, the movable end coordinates are expressed as

$$\boldsymbol{M}_{\mathrm{aM}}^{i} = \boldsymbol{T} \cdot \boldsymbol{M}_{\mathrm{aM}}^{i,0} + \boldsymbol{d}_{1}^{M} \tag{12}$$

The readings of the displacement transducers form a vector as

$$\boldsymbol{d}_{\mathrm{LVDT}}^{M} = \begin{bmatrix} d_{\mathrm{LVDT}}^{1} & d_{\mathrm{LVDT}}^{2} & \dots & d_{\mathrm{LVDT}}^{p} \end{bmatrix}^{T} \tag{13}$$

where p is the total number of displacement transducers. Obviously, the simultaneous equations of Eqs. (11) and (13) are associated with the CP displacements. As recommended by Molina *et al*. (1999), the CP displacements can be computed using iteration schemes; a solution in a least-squares sense can be obtained with readings of more transducers than the number of the CP DOF. In view of the transducer measurement error owing to the spherical hinge gaps, least-squares solutions enhance the measurement accuracy and reliability of the CP displacement. Therefore, this study always employs four transducers to measure the CP displacement. Notably, the layout of the displacement transducers influences the convergence of the iterative process. Wu *et al*. (2020) analyzed this layout issue and provided very helpful suggestions.

2.4 Iteration-based displacement command updating

The measured displacements are normally inconsistent with the desired displacements of the specimen, owing to the specimen bottom slip and/or connector deformation. To accurately reproduce desired displacements, outer-loop loading methods are extensively used in hybrid tests (Xu *et al*. 2017, Bonnet *et al*. 2007). A Newton-iteration-based method to update the actuator displacement commands was conceived (Wang *et al*. 2019b), as shown in Fig. 1, thereby forming a high-precision outer-loop strategy for loading the desired displacements.

A loading strategy in a BHS is intended to enforce the measured displacements of the CP to approach the desired displacements in a reasonable manner, that is

$$\boldsymbol{d} - \boldsymbol{d^M} = \boldsymbol{0} \tag{14}$$

For each integration step, the desired displacements are determined, whereas the measured displacements change in response to the continuous loading of the actuators. The measured specimen displacements can be regarded as a function of actuator commands as follows

$$\boldsymbol{d}^{M} = \boldsymbol{d}^{M}(\boldsymbol{d}^{C}) \tag{15}$$

Theoretically, the actuator displacement often differs from its command owing to loading system dynamics, gaps, bearing slips, and elastic deformation of the connector between the actuator and the specimen. These differences indicate that the CP displacement $\boldsymbol{d}^{M}$ is impossibly explicitly expressed by the command. On the other hand, the CP displacement $\boldsymbol{d}^{M}$, as responses to specific commands, can be measured. Consequently, updating actuator commands for loading is equivalent to the process of solving the nonlinear simultaneous equations of Eqs. (14) and (15). Based on the Newton iteration, the solution-seeking process can be expressed by means of

$$\boldsymbol{d}_{j+1}^{C} = \boldsymbol{d}_{j}^{C} + \left(\frac{\partial \boldsymbol{d}^{M}}{\partial \boldsymbol{d}^{C}}\right)^{-1} [\boldsymbol{d} - \boldsymbol{d^M}(\boldsymbol{d}_{j}^{C})] \tag{16}$$

where j represents the j-th iteration step. As $\boldsymbol{d^M}$ is not explicitly expressed as functions of $\boldsymbol{d}_{j}^{C}$, $(\frac{\partial \boldsymbol{d^M}}{\partial \boldsymbol{d^C}})^{-1}$ is replaced with $\frac{\partial \boldsymbol{d^C}}{\partial \boldsymbol{d^M}}$, which is approximated by $\frac{\partial \boldsymbol{d^A}}{\partial \boldsymbol{d^M}}$ evaluated according to Eq. (4), namely

$$\boldsymbol{J} = \frac{\partial \boldsymbol{d}^{A}}{\partial \boldsymbol{d}^{M}} = \begin{bmatrix} \frac{\partial d_{1}^{A}}{\partial d_{x}^{M}} & \frac{\partial d_{1}^{A}}{\partial d_{y}^{M}} & \frac{\partial d_{1}^{A}}{\partial d_{\theta}^{M}} \\ & \cdots & \\ \frac{\partial d_{n}^{A}}{\partial d_{x}^{M}} & \frac{\partial d_{n}^{A}}{\partial d_{y}^{M}} & \frac{\partial d_{n}^{A}}{\partial d_{\theta}^{M}} \end{bmatrix} \tag{17}$$

in which $\boldsymbol{J}$ means a Jacobian matrix, indicating a matrix of the partial derivatives of the actuator displacements with respect to the components of the CP displacements. In view of the difference between $\boldsymbol{d^C}$ and $\boldsymbol{d^A}$, a reduction factor is introduced to the Jacobian matrix; hence, the final iterative scheme yields

$$\boldsymbol{d}_{j+1}^{C} = \boldsymbol{d}_{j}^{C} + \alpha \boldsymbol{J}[\boldsymbol{d} - \boldsymbol{d}^{M}(\boldsymbol{d}_{j}^{C})] \tag{18}$$

where α is the reduction factor between 0 and 1. Eq. (18) indicates that the same reduction factor is applied to all the actuators. In order to accommodate different loading errors of different actuators, α can be set as a diagonal matrix. In the implementation, it is necessary to define an iteration convergence criterion, which is not elaborated on here.

As shown in Eq. (18), this loading strategy accounts for the nonlinear relationship between the actuator elongation and the CP displacements by including the term $\boldsymbol{J}$, and displacement deviations in all directions simultaneously contribute to the command increment. Compared with the existing methods in which $\boldsymbol{J}$ is not considered, the new loading strategy is suitable for large-deformation problems, possesses higher accuracy and faster convergence, and allows a simpler parameter adjustment process. Moreover, given the uncertainty in tests, the reduction factor leads to smoother loading for the CP displacement. In view of these advantages, this new loading strategy is more promising.

2.5 Optimal forces of actuators

In a BHS, when the specimen size and/or stiffness is large, it is often difficult to achieve the loading objective by only using three actuators due to the limitation of their loading capacities. When more than three actuators are used, the actuators often interfere with each other, in that loading rates and errors of different actuators are often different; and thus, the loading may be ineffective. Ineffective loading here means that parts of the actuator forces do not induce specimen deformation, but counteract each other in the specimen floor. As an extreme example, one actuator may hinder loading, that is, the remaining actuators need to resist this actuator force. Actually, the CP displacements can be realized by using three displacement-controlled actuators, whereas additional actuators (referred to as redundant actuators) should not influence these displacements. Instead, redundant actuators affect the distribution of the specimen restoring force among the actuators. Therefore, measures have to be taken to avoid ineffective loading and to optimize the force distribution among actuators.

A previous study (Molina *et al*. 1999) implemented displacement control for redundant actuators by optimizing the output force according to a performance index. Similarly yet differently, this new strategy adopts direct force control for redundant actuators with a more concise optimization performance index to avoid solving nonlinear equations, as shown in Fig. 1.

The optimization objective is that the actuator force is far from its loading capacity and that the sum of the absolute values of all actuator forces is minimum. This objective is intended to prevent suspending BHS owing to an actuator with a weak loading capacity generating output force beyond its limit, and thus to maximize the total loading capacity of the testing system. The optimization objective is defined as

$$\min h(\mathbf{F}_L) = \sum_{i=1}^{n} \left(\frac{f_L^i}{f_m^i}\right)^2 \tag{19}$$

where f_L^i and f_m^i are the optimal force and loading capacity of the i-th actuator, respectively, and $\mathbf{F}_L = [f_L^1 \quad f_L^2 \quad \cdots \quad f_L^n]^T$. One advantage of minimizing this summation is to minimize the total actuator force to the only necessary amount, where the ineffective loading is, therefore, minimized. Notably, the resultant forces of these optimal forces are the restoring force of the specimen, that is, the static equilibrium conditions in the three directions are the constraint conditions of this optimization problem. In the loading scheme of n actuators, three displacement-controlled actuators are used to ensure the accuracy of the CP displacement, whereas the remaining (n-3) actuators are redundant and manipulated in force mode.

To solve for the extrema under these constraint conditions, the Lagrangian multiplier method is adopted in this study. Implementation of this method gives simultaneous equations about optimal forces and multipliers as

$$\begin{bmatrix} \boldsymbol{B} & -\boldsymbol{A}^T \\ \boldsymbol{A} & \boldsymbol{0} \end{bmatrix} \begin{bmatrix} \boldsymbol{F}_L \\ \boldsymbol{\lambda} \end{bmatrix} = \begin{bmatrix} \boldsymbol{0} \\ \boldsymbol{r} \end{bmatrix} \tag{20}$$

where

$$\boldsymbol{B} = \begin{bmatrix} \frac{2}{(f_m^1)^2} & 0 & \cdots & 0 \\ 0 & \frac{2}{(f_m^2)^2} & \cdots & 0 \\ \cdots & \cdots & \cdots & \cdots \\ 0 & 0 & \cdots & \frac{2}{(f_m^n)^2} \end{bmatrix} \tag{21}$$

$$\boldsymbol{\lambda} = [\lambda_1 \quad \lambda_2 \quad \lambda_3] \tag{22}$$

in which λ is a Lagrangian multiplier. It can be observed that, differently from Molina *et al*. (1999), the optimization problem is transformed into an easy problem of solving linear simultaneous equations. This improvement is attributed to the new performance index in Eq. (19). As different performance indexes result in different optimal forces, designing an appropriate performance index is very significant for BHS.

2.6 Force-based loading of redundant actuators

In the new loading strategy, the redundant actuators are operated in force control mode, that is, they can directly track optimal forces as calculated. When the optimal forces of the redundant actuators are achieved, in view of the equilibrium conditions, all other actuators automatically accomplish their optimal forces.

Force control of redundant actuators has an advantage that there is no need to set any additional parameters for the redundant actuators instead of inner loop controller parameters; consequently, the loading strategy is very straightforward and easy to realize. Furthermore, common concerns regarding force control are that it is more challenging to achieve force target contents of the specimen frequency owing to natural velocity feedback (Zhao *et al*. 2003), and might be instable when the specimen has a negative stiffness. In fact, the former phenomenon only exists in dynamic force loading, whereas this study adopts a quasi-static loading manner and thus is free of this concern. For the latter one, redundant actuators are only intended to distribute the actuator forces reasonably without affecting the CP displacement. The CP displacement is ensured by the three displacement-controlled actuators. Therefore, even with a negative stiffness specimen, the new loading strategy is still free of the instability problem. The above characteristics of the force control of redundant actuators are well confirmed by numerical simulations, validation tests and its application to a full-scale test presented in the following sections.

3. Virtual bi-directional hybrid simulations (vBHS)

3.1 Structure model

The emulated structure was a dynamic system in consideration of three DOF, namely translations in X and Y directions and rotation with respect to the third direction, as shown in Fig. 3. The masses and the moment inertia were 2.56×10^6 kg, 2.56×10^6 kg and $1.69 \times 10^6 \text{kg} \cdot m^2$, respectively. The restoring forces of this structure were modeled by three springs, including one along X direction and two along Y direction. The relative positions between the CP, the springs and the coordinate system are depicted in Fig. 3. In the linear vBHS (referred to as Case 1), stiffnesses of three springs were supposed as 9.9×10^7N/m. For simplifying the analysis, the coupling of restoring forces between X direction and the other two DOFs was neglected, and the restoring force coupling in Y and rotational directions was linearized. These led to the structural natural frequencies of 0.99 Hz (in X direction), 1.36 Hz and 2.13 Hz. The damping ratio in X direction was assumed as 2%; Rayleigh damping was adopted for the other two DOFs with two modal damping ratios of 2%. In the vBHS (referred to as Case 2) with a bi-linear specimen, all springs were simulated by means of bi-linear models characterized in a first stiffness of 9.9×10^7N/m, a second stiffness of 2.97×10^7 N/m and a yielding displacement of 0.005 m. In the strongly nonlinear vBHS (referred to as Case 3), springs were represented by tri-linear models with a first stiffness of 9.9×10^6 N/m, second and third stiffness ratios of 0.5 and -0.2, crack and yielding displacements of 0.01 m and 0.02 m, and a degradation coefficient of -0.4 for the unloading stiffness, respectively. Structural damping in Case 1 was also employed in Case 2. In both cases, the structure was subjected to El Centro bi-directional earthquake record. In particular, EW and NS directions of the earthquake were applied along X and Y axes with the peak ground accelerations scaled to 52.54 Gal (X) and 70 Gal (Y).

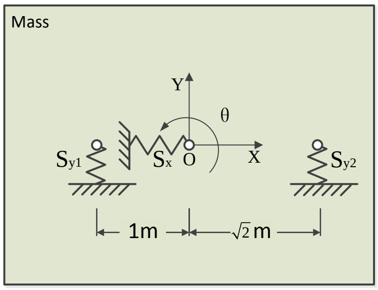

Fig. 3 Schematic of the emulated structure

In vBHS, the emulated structure was partitioned into numerical and virtual physical parts in the traditional PDT manner. In particular, the masses and damping were numerically simulated while all springs were virtually loaded through numerical models of actuators controlled in displacement and/or force mode. The equation of motion of the emulated structure was discretized by means of the central difference method with a time interval of 10 ms.

3.2 Models and layout of actuators

In order to reliably reveal the performance of the loading strategy, this study took into account distinct

Table 2 Parameters adopted in vBHS

Variable	Value	Description
C_F	78.74 V/m	Conversion factor for displacement control
K_s	0.1	Equivalent servo-valve gain
K_v	1.60×10^{-2} m^3/sec	Main-stage servo-valve flow gain
K_a	3.0×10^{-12} m^5/N/sec	Coefficient related to fluid compressibility in actuator
C_l	1.0×10^{-12} m^5/N/sec	Leakage coefficient in actuator
A	8.21×10^{-3} m^2	Actuator piston area
k_p	100	Proportional gain for displacement control
k_i	10	Integral gain for displacement control
CF_1	5.6×10^{-5} V/N	Conversion factor for force control
K_p	0.5	Proportional gain for force control
K_i	0.01	Integral gain for force control
γ_1	$5.0\times10^5/k_0$	Gain for displacement command correction with $k_0 = 9.9\times10^7$ N/m
γ_2	$1.0\times10^{-4}/k_0$	Gain for displacement command correction with $k_0 = 9.9\times10^7$ N/m
f_m	2.0×10^6 N	Load capacity of actuators
α	0.6	Coefficient for displacement command of new loading strategy
T_c	0.001 s	Sampling time for control
T_u	0.1 s	Time interval for updating actuator commands
T_l	1 s	Loading time for desired displacements of each integration step

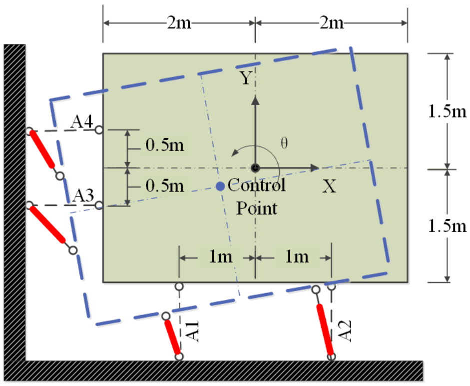

Fig. 4 Layout of actuators

dynamic characteristics and loading capacities of actuators. Actuators in both force and displacement mode were modeled along the line of Zhao *et al*. (2003). These models contained signal conversions, a servo-valve model, a main stage servo-valve model, fluid compressibility and leakage and a natural velocity feedback loop. Actuator properties along with other parameters adopted in vBHS were listed in Table 2.

The layout, number, and coordinates of actuators are depicted in Fig. 4. To consider the frequently- encountered issue that different types of actuators have to be employed in one test, PI parameters of displacement control for A2 were reduced to one half for simulating different actuator response rates in both cases, and loading capacity of A1 in Case 2 was assumed as 100 t, one half of other actuator capacities. Furthermore, in the vBHS with the new strategy, A4 was operated in force control mode while all other actuators ran in displacement mode.

For the purpose of revealing advantages of distinct methods for ineffective force compensation, a displacement command correction method similar to Molina *et al*. (1999) was adopted. This method updates redundant actuator displacement commands by adding an increment relevant to the ineffective force, namely

$$\begin{aligned} \Delta F_{j+1} &= \Delta F_j + (f_j^4 - f_{L,j}^4) \\ d_{j+1}^{CC} &= d_{j+1}^C - \beta\frac{\Delta F_{j+1}}{K_a} = d_{j+1}^C - \gamma\Delta F_{j+1} \end{aligned} \tag{23}$$

where $f_{L,j}^4$, f_j^4 and ΔF_j denote the optimal force, actual force and accumulative ineffective force of A4 at the j-th sampling step, respectively; K_a stands for the specimen stiffness along the actuator direction, namely the derivative of the actuator force with respect to actuator displacement; β and γ are two reduction factors, and $\gamma = \frac{\beta}{K_a}$; d_{j+1}^C is the displacement command evaluated by Eq. (18), while d_{j+1}^{CC} represents the corrected displacement command. Apparently, this method reduces the ineffective force by adjusting the actuator displacement response via its command correction. The parameter K_a is related to the specimen stiffness and the actuator direction. Actually, specimen nonlinearity and actuator rotation can result in variation of this stiffness. Consequently, an appropriate parameter is often required to be tuned according to real specimen properties and actuator trajectory. In vBHS using this method, four actuators were operated in displacement control mode with A4 command corrected by means of Eq. (23).

3.3 Simulation results

(1) Case 1: linear specimen model

Fig. 5 depicts the comparison of displacement time histories obtained with four actuators controlled in displacement mode without command correction for ineffective force compensation. As aforementioned, ineffective force compensation ensures the effectiveness of actuator forces and tends not to affect desired displacement tracking of the specimen. As a result, displacements obtained without compensation are presented here to demonstrate the tracking performance of the new loading strategy. As shown in the figure, three response displacements accurately matched the desired displacements at the end of the loading steps. Given the geometric nonlinearity due to specimen rotation and difficulty resulted from different actuator response rates due to controllers, this result reflected the efficiency and accuracy of the new loading strategy for coupling displacement control. To further analyze the tracking performance, two indicators, i.e., the maximum absolute synchronization error (MASE) and the normalized root mean square error (NRMSE) (Wang *et al*. 2020), were evaluated and collected in Table 3. It can be seen that there were no great differences among the results of the three simulations. This showed that compensations had little influence on displacement response accuracy. Moreover, negligible errors between desired and actual displacements,

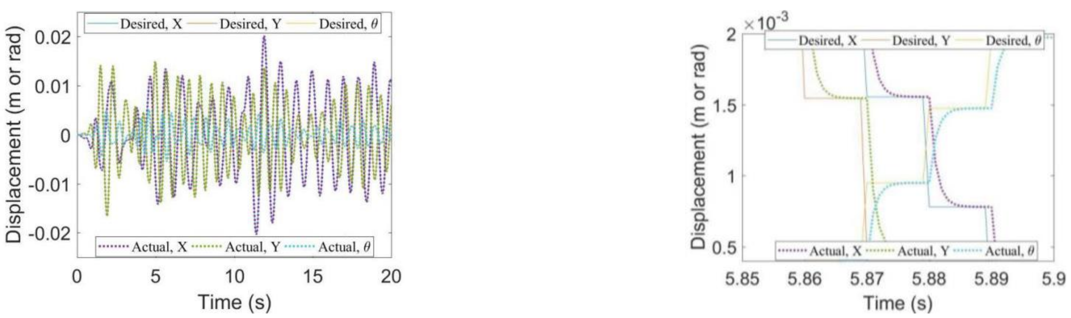

(a) Global view (b) Close-up view

Fig. 5 Comparison of displacement time histories obtained without ineffective force compensation

Table 3 Performance indicators for vBHS

Method	MASE			NRMSE		
	X (×0.01 mm)	Y (×0.01 mm)	Theta (×1.0×10^{-5} rad)	X (×0.1%)	Y (×0.1%)	Theta (×0.1%)
Without compensation	5.59	4.67	2.51	2.52	3.10	4.73
Displacement command correction	5.58	4.68	2.51	2.52	3.10	4.73
New loading strategy	5.80	4.57	2.65	2.54	3.04	5.17

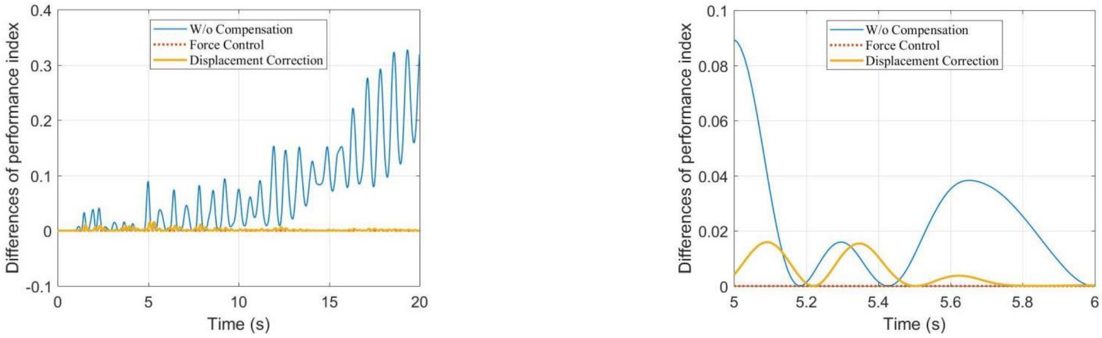

(a) Global view

(b) Close-up view

Fig. 6 Differences of performance index h (quadratic sum of normalized forces) in Eq. (19)

(a) Global view

(b) Close-up view

Fig. 7 Time histories of actuator forces

between desired and referenced displacements, validated the outstanding accuracy of the new loading strategy.

Fig. 6 illustrates index discrepancies in three simulations, which are defined as the difference between the actual and optimal indexes h in Eq. (19). In the figure, ‘Force Control’ stands for results obtained with the new loading strategy, while ‘W/o Compensation’ denotes that obtained using four displacement control actuators without ineffective force compensation. Greater discrepancy indicates more ineffectiveness of actuator forces in the sense of the index. In contrast to the vBHS without compensation, the displacement correction method and the new loading strategy exhibited remarkable compensation performance. In fact, the largest discrepancies of three simulations were 0.33, 7.53×10^{-6}, 0.016, respectively. The new loading strategy showed its advantage over the displacement correction method. A larger parameter γ for the correction could result in a smaller error. Moreover, this figure showed that the discrepancy of the case without compensation continuously drifted. This meant that the actuator forces were more and more ineffective as the simulation was advancing. One can speculate that, as long as the time duration of the simulation is long enough, the test must be suspended since the actual force reaches its loading capacity. This shows that ineffective force compensation plays a significant role in complex BHS and bi-directional quasi-static tests loading with redundant actuators.

Time histories of actuator forces of A1 and A2 are plotted in Fig. 7, as well as the optimal force of A1. One can observe that the force of A1 obtained with the new strategy matched the optimal one very well, indicating the loading was effective in the index sense. Meanwhile, the force of A1 obtained without compensation tended to be larger than the optimal one, and the error between them seemed to gradually increase. This is consistent with that revealed in Fig. 6. With the increase in A1 force, A2 force decreased to ensure the translational displacement response in the Y direction of the CP.

(2) Case 2: bi-linear specimen model

Accurate loading for Case 2 was much more challenging

(a) Global view

(b) Close-up view

Fig. 8 Comparison of displacement time histories obtained without ineffective force compensation

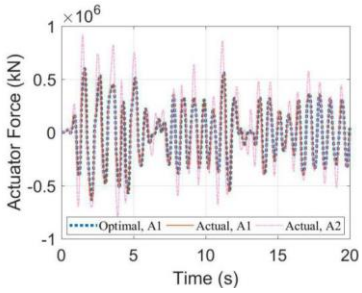

Fig. 9 Time histories of actuator forces obtained with the new loading strategy

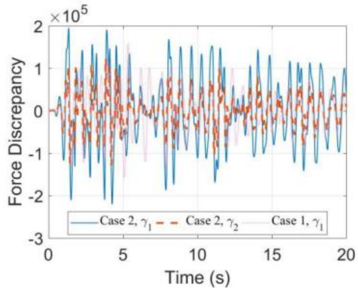

Fig. 10 Ineffective forces of A4 in different cases

than Case 1 owing to specimen nonlinearity and various actuator loading capacities. In this case, springs of the structure were simulated by means of a bi-linear model, and the loading capacity of A1 was set as one half of other actuators. In spite of these, the new loading strategy performed considerably well in terms of its loading accuracy of the CP displacements and its force distribution optimization among actuators. Similarly to Case 1, results obtained without any special treatment to the redundant actuator are presented as a representative, as shown in Fig. 8. According to the optimization index, the optimal force of A1 must be smaller to enforce it far away from its capacity. Hence, a moment was induced between A1 and A2, and was balanced among all actuators. Outstanding tracking performance verified that the new strategy is capable of loading for complicated and demanding cases. Notably, for saving space, indicators in Case 2 in accordance with Table 3 are not presented; virtually, conclusions consistent to those in Case 1 can be drawn here.

Force time histories of A1 and A2 obtained with the new loading strategy are illustrated in Fig. 9, as well as the optimal force for A1. Good agreement between the actual and optimal forces of A1 was observed, which indicated the effectiveness of the new loading strategy for the redundant actuator. Actually, this new loading strategy directly imposes this optimal force to the specimen via actuator force control. Therefore, this strategy requires no additional parameters, and hence, is straightforward and easy to implement. Moreover, force control in slow tests can achieve very accurate loading, as illustrated in this figure. In Fig. 9, peak forces of A1 were always less than those of A2, in that the loading capacity of A1 was supposed as one half of A2. To avoid the case where the test had to be suspended since the actual force of A1 reaches its capacity, the optimization algorithm tended to reduce the optimal force of A1. Numerical results in Fig. 9 match this understanding. However, the cost of optimization was to induce an internal resultant moment owing to A1 and A2, which was not imposed onto the specimen but was balanced by the other two actuators. Consequently, the force distribution was optimized solely in the sense of the specific performance index, and was often not optimal to some other performance indexes. Designing suitable actuator layout and a performance index according to actuator properties and potential specimen responses are of great importance to BHS. The diversity of actuator properties and layout is the unique feature of BHS, distinct from shaking table tests.

Fig. 10 depicts the ineffective forces of A4 in different cases obtained with the displacement correction method, which is defined as the difference between the actual and optimal forces. The ineffective force in Case 2 was larger than that in Case 1 with the same parameter γ_1. In Case 1, the ineffective force was small and then the compensation was relatively easy. In Case 2, the ineffective force was large owing to different actuator capacities. Meanwhile, the nonlinearity of the specimen in Case 2 could lead to a smaller equivalent stiffness along the actuator direction. Consequently, there was a greater difference between this equivalent stiffness and the one adopted for the parameter γ_1, which implied worse compensation performance. In order to enhance the performance, a larger parameter, $\gamma_2 = 0.0001/k_0$, was adopted with results presented in Fig. 9 and verified its effectiveness. These simulations show that an appropriate parameter has to be chosen considering the specimen stiffness, actuator movement, loading capacities and so on. In contrast, the new loading strategy requires no outer loading loops for the redundant actuator.

Fig. 11 demonstrates index discrepancies obtained using the new loading strategy, the displacement correction

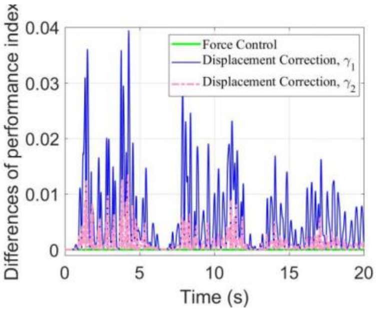

Fig. 11 Differences of performance index h (quadratic sum of normalized forces) in Eq. (19)

method with γ_1 and γ_2. Obviously, the new loading strategy outperformed the other two, and the displacement correction with γ_1 was the worst. This is consistent with that in Fig. 9.

(3) Case 3: tri-linear specimen model

This strongly nonlinear vBHS was carried out to validate the performance of the new loading strategy considering strain-hardening/softening and negative-stiffness properties of the specimen. These simulations are considerably challenging for its demanding control precision, in that actuator overshoot and oscillation induce undesirable loading-unloading hysteretic loop and hence, inaccurate structural responses. In view of this and to obtain more smooth responses, the reduction factor α in Eq. (18) was reduced to 0.1 and the inner loop control parameters of actuators were diminished to 1% for displacement and 10% for force. The time interval for updating actuator commands and loading time for desired displacements of each integration step, namely T_l and T_u, are set 3 s and 0.05 s, respectively. Moreover, not only specimen hysteretic loop but also specimen mass and damping were taken into account in this case, with the mass of 100 and damping of 8000 (in international units) for each DOF. To effectively excite the structure, the earthquake records in two directions are tuned to 75.1 Gal (X) and100 Gal (Y).

A comparison of hysteretic loops of Spring X and Y2 with reference ones are depicted in Fig. 12. One can see that both springs exhibit strong nonlinearities, e.g., the negative stiffness behavior. The hysteretic loops obtained in vBHS with the new loading strategy are in good agreement with the reference ones, indicating favorable loading accuracy. These results verify the insights abovementioned that the new loading strategy is still free of the instability problem even with a negative stiffness specimen. Displacement time histories of three DOFs are compared with reference ones in Fig. 13, where the coincidence of time histories validates the excellent tracking performance of the new loading strategy.

One can draw conclusions from these simulations that the new loading strategy is capable of accurately reproducing the desired displacements, and straightforward and easy to implement for optimizing the force distribution. Although specimen nonlinearity, geometric nonlinearity, different actuator response rates, different loading capacities were taken into account, the new loading strategy performed

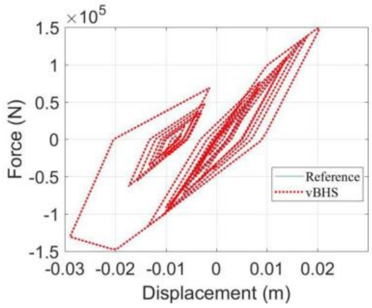

(a) Spring X

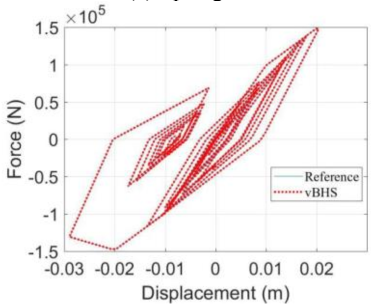

(b) Spring Y2

Fig. 12 Hysteretic loops of Spring X and Y2 obtained in vBHS of Case 3

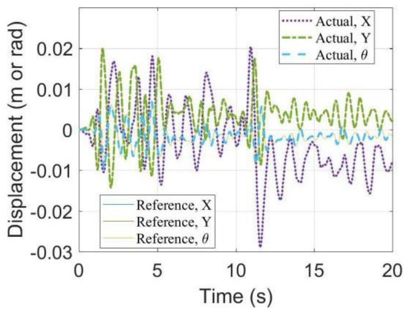

Fig. 13 Displacement time histories of the structure obtained in Case 3

satisfactorily. The displacement correction method was also effective for loading of the redundant actuator as long as an appropriate parameter was set.

4. Verification tests of the new loading strategy for BHS

4.1 Hybrid test platform: HyTest

A BHS involves structural response evaluation by using step-by-step integration algorithms, loading the desired displacements, solving for the CP displacement, the composition of the specimen restoring forces, and loading for the redundant force. Therefore, successful implementation of a BHS relies on reliable specialized test software. In this study, the new loading strategy was integrated into a hybrid test software - HyTest - for performing verification and application tests. HyTest is a hybrid test platform developed at Harbin Institute of Technology (Yang *et al*.

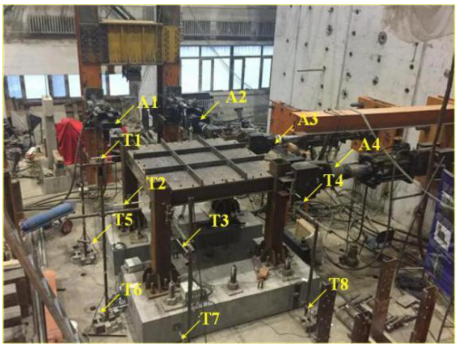

Fig. 14 Specimen and layout of the equipment

2017). It consists of three primary modules, i.e., a coordinator, a numerical substructure module, and a loading module. The coordinator is responsible for solving equations of motion of the emulated structure, the numerical substructure module is designed for analysis of the NS and communicating with finite element software, and the loading module is to generate actuator commands for accurately imposing the desired displacements to the specimen.

4.2 Structural model, test equipment, and parameters

The prototype was a single-story steel frame. The mass and damping matrixes are supposed diagonal, with the diagonal elements of m^3/s 2.56×10^6 kg, 2.56×10^6 kg, 1.69×10^6 kg·m^2, and 6.37×10^5 N·s/m, 6.37×10^5 N·s/m, 1.27×10^6 N·s/rad, respectively. The specimen was a single-story single-bay steel frame with the dimensions of 2,000 mm × 2,000 mm × 1,400 mm (length × width × height). The frame was made of Q235B steel, and the columns were square steel tubes each with the dimensions of 250 mm × 250 mm × 10 mm; I-beams with the dimensions of HN 250 mm × 125 mm × 9 mm × 6 mm were deployed. The specimen floor was made of a steel plate with a thickness of 30 mm. To prevent the specimen floor from undergoing large deformation, two stiffeners with a height of 150 mm were welded on the steel plate in both longitudinal and lateral directions. The specimen was constructed using a geometric scale factor of 1: 2 with respect to the prototype.

The specimen and layout of the actuators and displacement transducers are shown in Fig. 14. Four MTS actuators were used for loading, including two 1000 kN actuators arranged in the Y direction, and one 1000-kN

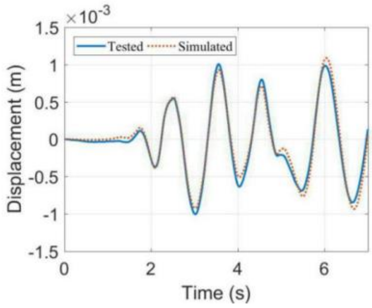

(a) Comparison of tested and simulated results in the X direction

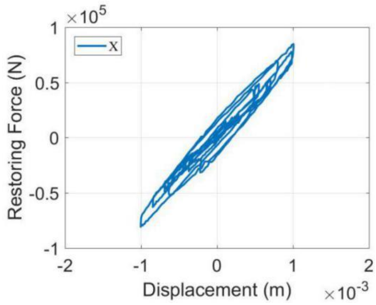

(b) Force-displacement relationship in the X direction

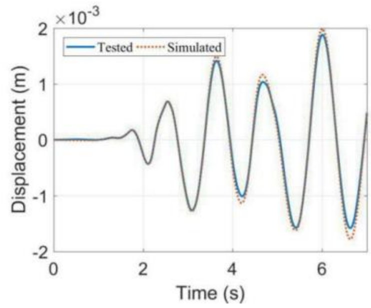

(c) Comparison of tested and simulated results in the Y direction

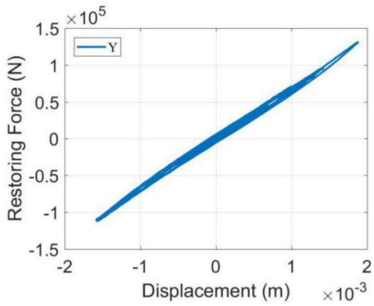

(d) Force-displacement relationship in the Y direction

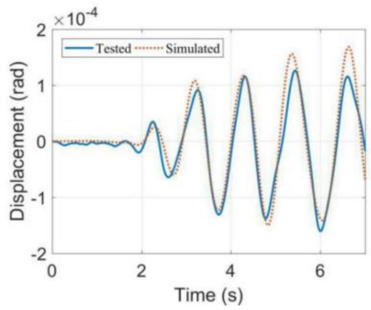

(e) Comparison of tested and simulated results in the rotational direction

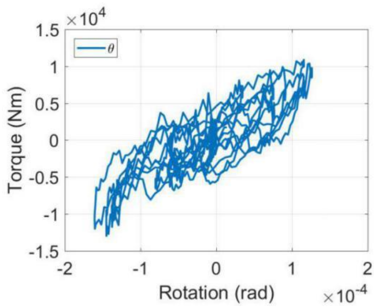

(f) Force-displacement relationship in the rotational direction

Fig. 15 Comparison of tested and simulated displacements and force-displacement curves actuator and one 2000-kN actuator in the X direction. Eight linear variable differential transformer (LVDT) displacement transducers were arranged to measure the displacement of the specimen, consisting of four 5-mm displacement transducers arranged on the ground beams to measure the overall slip of the specimen, and four 10-mm displacement transducers arranged on the specimen to measure the specimen displacement relative to the strong floor.

The El Centro earthquake record (1940, NS) was scaled to a peak ground acceleration of 3.5 Gal, and only the first 7 seconds of the record was adopted to excite the emulated structure in two translational directions in that one actuator encountered a lack of oil pressure. The central difference method with a time interval of 0.01 s was chosen as the time integration algorithm. The configuration information of actuators and displacement transducers, MTS channel allocation were typed to the loading module of HyTest, which communicated with the MTS loading system. The maximum number of iterations for loading desired displacements of each integration step was 10, and the loading time of each iteration was 0.5 s.

4.3 Test results

The new loading strategy was tested to examine its performance of tracking the desired displacements of the specimen and optimizing force distribution. The commands of actuators in displacement mode were updated using the iteration-based approach abovementioned. The redundant actuator was operated in force mode wherein the actuator force in the previous sampling step was used to calculate the optimal force, which was then sent as the force command to the redundant actuator for implementation.

Investigations showed that the maximum translation error in both directions was about 1.0×10^{-2} mm, and the maximum rotation error was about 1.0×10^{-6} rad, indicative of the relatively high accuracy of the loading scheme. The stiffnesses of the specimen were estimated using the measured data in the test, and the structural dynamic responses were obtained through time history analysis, which was compared with the desired displacements of the test, as shown in Fig. 15. It can be observed that the test results, in general, were consistent with the time history analysis results, and thus, the test data were reasonable. The best consistency was observed in the Y direction. There was a certain degree of inconsistency in the rotational DOF, which might be attributed to the fact that, due to the small rotation angle, the test error has a higher influence on the rotational displacement than the translational displacement. As shown by the force-displacement relationship curves, the actual behavior of the specimen was not completely linear elastic, and thus, time-history analysis results based on the linear elastic assumption should deviate from the test results to some extent.

The displacements of the two actuators along the Y direction were averaged and compared with the average of the specimen displacement measured using two displacement transducers in this direction, as shown in Fig. 16. Apparently, the actuator average displacement was significantly larger than the transducer-measured specimen displacement, with the error at around 3.6 s up to 1.5 mm. This observation showed that the actuator displacement was significantly different from the specimen displacement, and it would be impossible to obtain accurate and reliable test results without using an outer-loop loading strategy. Similar results were obtained in the X direction and are omitted for saving space.

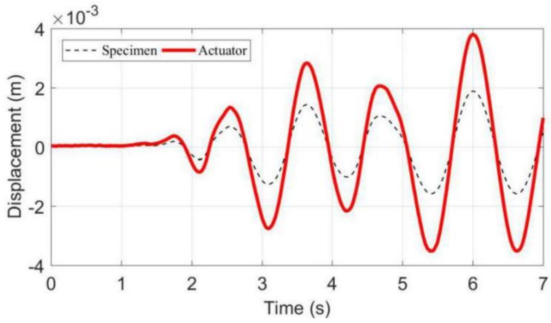

Fig. 16 Actuator and specimen displacements in the Y direction

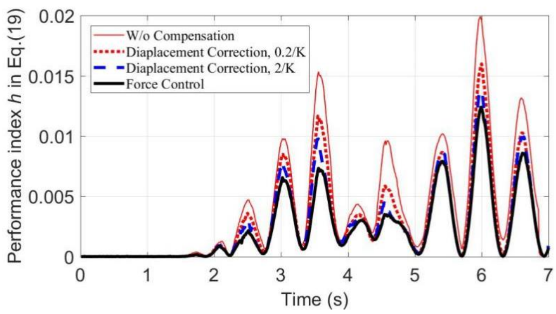

Fig. 17 Comparison of performance index h (quadratic sum of normalized forces) in Eq. (19)

To compare the performance of different redundant actuator loading methods, the performance index h was calculated using the measured forces of the actuators obtained with different methods, as shown in Fig. 17. In the figure, K denoted the estimated specimen stiffness in the preliminary test. The results showed that both the force control method and the displacement command correction for the redundant actuator achieved force distribution optimization, with the former method exhibiting better optimization performance. For the displacement correction method, its performance relies on its parameter, indicating that cautious parameter tuning is required for complex BHS. In Fig. 17, the curves of different loading methods almost overlapped in the first 2 s, which was attributed to the fact that the output force of the actuators was very small in this time range, and thus, there was limited interference among actuators.

5. Application of the new loading strategy to BHS on a full-scale two-story specimen

The new mixed force-displacement loading strategy was applied to BHS on a full-scale two-story reinforced concrete frame with buckling-restrained braces (RCF-BRB). The prototype structure was an eight-story RCF-BRB, which

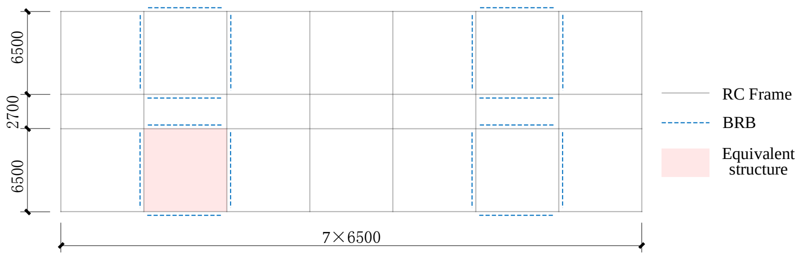

Fig. 18 Plan layout of the prototype structure (unit: mm)

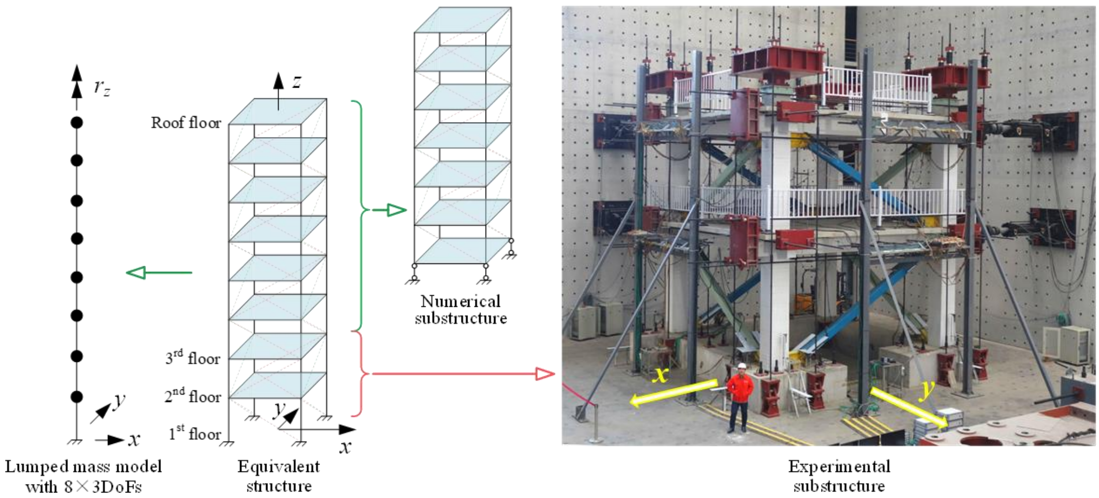

Fig. 19 Model of the BHS

was seven-span in length and three-span in width, as shown in Fig. 18. Except the first story with a height of 3.9 m, each story was 3.5 m in height. The frame was assumed to be built in an area where the seismic design parameters are a seismic intensity of 8, a site category of Class II, and a design earthquake type of Group I as specified in the Chinese Code for Seismic Design of Buildings (GB50011-2010, 2016). To simplify the boundary conditions and facilitate modeling, the shaded part in Fig. 18 was chosen for the BHS. To accurately reproduce the seismic response of the prototype structure, it was necessary to adjust the mass of the shaded part so that the first and second periods and modes of vibration were close to those of the prototype structure, and such an adjusted structure was named the equivalent structure. Further information related to this test can be found in Wu *et al*. (2020) and Tan *et al*. (2020).

Numerical analysis results showed that the maximum inter-story drift ratio (IDR) was present at the second story. Therefore, the bottom two stories of the equivalent structure were selected as the PS, whereas the upper six stories, referred to as the NS, were simulated using *OpenSees* (Mazzoni *et al*. 2006) as shown in Fig. 19. In the coordinator of HyTest, a differential equation of motion was established based on the lumped mass model of the equivalent structure. The central difference method was employed to obtain the CP displacements at each integration step. Then, the CP displacements of the bottom two stories and upper seven stories (refer to Fig. 19) was imposed on the PS and NS by the loading and numerical substructure modules of HyTest, respectively. The BHS was performed using the El Centro bi-directional earthquake record (1940, NS and EW). For each earthquake grade, the X direction earthquake record was first scaled with the peak to the specified value from GB50011-2010, and then the Y direction earthquake record was adjusted according to the original peak value ratio between the two directions.

The layout of the horizontal loading equipment and displacement transducers is shown in Fig. 20. To improve the loading capacity, four actuators were arranged at each floor, consisting of Actuators 1 to 3 controlled in displacement mode and Actuator 4 controlled in force mode. To reduce the measurement error, four displacement transducers were deployed on each floor. In accordance with the aforementioned loading and measurement methods, hinged bearings were used at both ends of the actuators and the displacement transducers.

The new loading strategy for BHS was carried out herein. The error tolerances for the two translations and the rotation in the loading strategy were set to 0.001 mm and 0.001 rad, respectively. To ensure smooth implementation of the test, the maximum number of command updating steps was set to 15, that is, if the error tolerance was still exceeded after 15 updating steps, the test proceeded to the next numerical integration step. During the test, the loading performance for the desired displacements was closely monitored at all times, and when necessary, the reduction factor α (in Eq. (18)) for the loading commands of the actuators was adjusted. The minimum reduction factor α used in the test was 0.6.

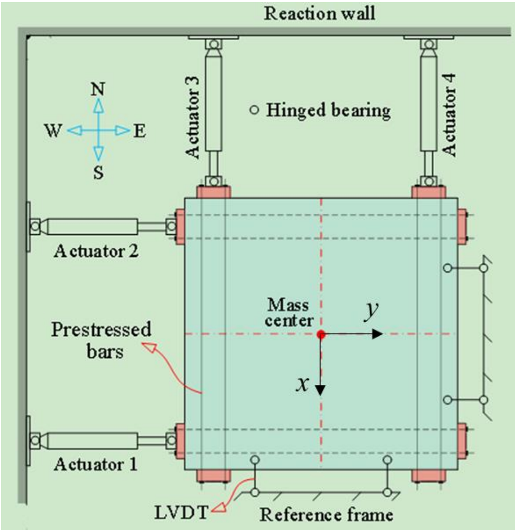

(a) Layout of actuators and LVDTs

(b) Close-up view of Actuators

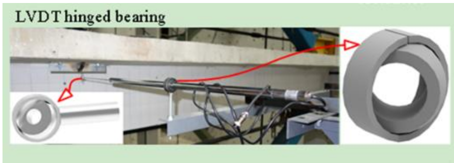

(c) Close-up view of LVDT hinged bearings

Fig. 20 Equipment for horizontal loading and measurement

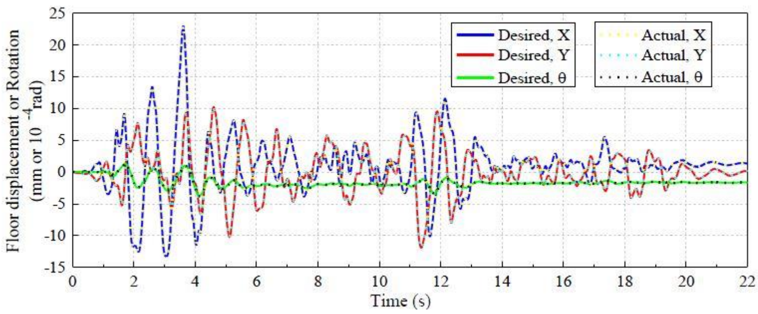

(a) Global view

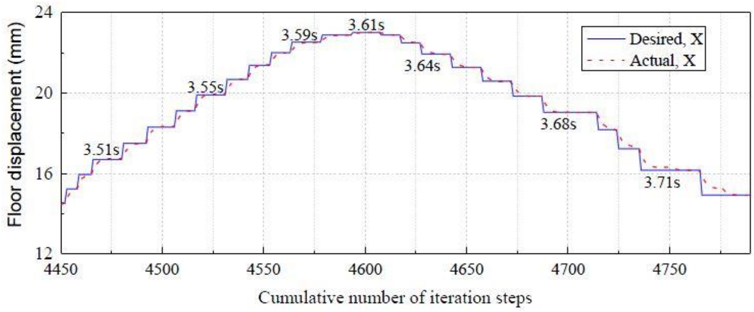

(b) Close-up view

Fig. 21 Displacement tracking performance of the second floor in BHS with 200 Gal earthquake

Figs. 21 and 22 show the tracking performance of the CP displacements of the second floor during the tests with a peak ground acceleration of 200 Gal (10%/50-year probability of exceedance) and 400 Gal (2-3%/50-year probability of exceedance), respectively. One can see that the measured CP displacements excellently tracked the desired displacements in a smooth and accurate manner. In Fig. 21(b)), the total updating numbers of different integration steps were variable, which was attributed to the fact that, at different test stages, the loading difficulties were distinct and hence, to achieve the same loading accuracy, the required command updating numbers varied. Although the rotational angles were considerably small, the tracking accuracy was outstanding. These results indicate the capability of the new strategy for large scale BHS.

Fig. 23 presents the actual actuator forces of the second floor at each loading step in the BHS of the two grades of earthquakes. As the rotation angles of the specimen were very small, the actual forces of the two actuators in the same direction were almost the same. The maximum force was about 1500 kN, up to 3/4 of the actuator loading capacity. These results showed that force control for the redundant actuator performed well and the ineffective forces were well controlled by the mixed force-displacement loading strategy. These application tests demonstrated that the new strategy is capable of accurately

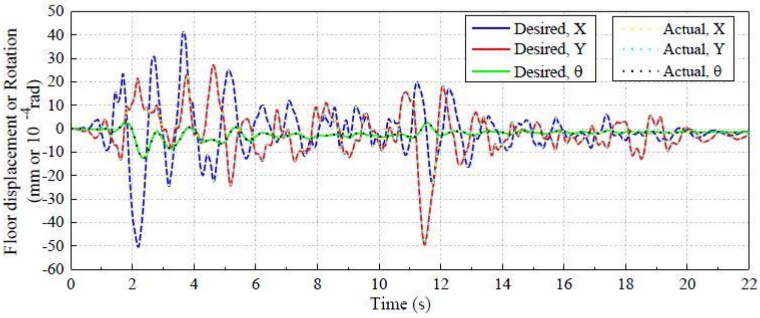

Fig. 22 Displacement tracking performance of the second floor in BHS with 400 Gal earthquake

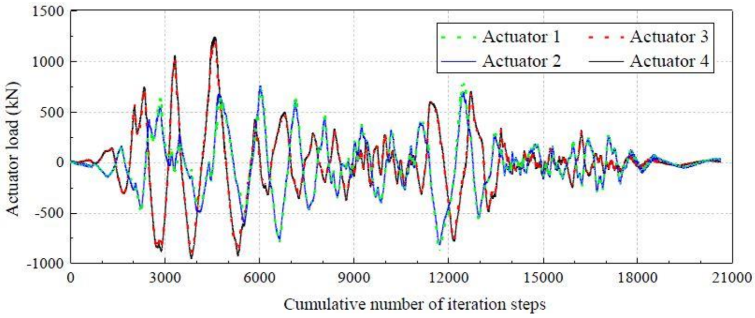

(a) Test with 200 Gal earthquake

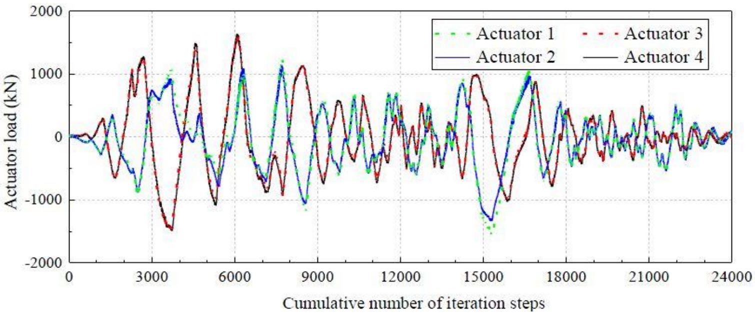

(b) Test with 400 Gal earthquake

Fig. 23 Actuator forces of the second floor

and effectively reproducing the desired displacements in large scale BHS.

6. Conclusions

This study investigated the performance of a new loading strategy for bi-directional hybrid simulations (BHS). This strategy consists of an iteration-based method for updating the actuator displacement command and a force-based loading for redundant actuators. Virtual BHS was performed in consideration of different loading rates and capacities of actuators, and specimen material nonlinearity. With the assistance of hybrid test software - HyTest - integrated the new strategy, validation tests on a steel frame and application tests on a full-scale two-story frame structure were carried out. The main conclusions drawn from this study are as follows:

- This new loading strategy updates actuator displacement commands based on actual displacements of the control point (CP), the previous actuator commands and the nonlinear relationship between the CP displacements through the Jacobian matrix. The actual CP displacements are solutions in a least-squares sense using the readings of four displacement transducers, which can minimize the measurement errors. The adopted Jacobian matrix transforms the CP displacement deviations in all directions to commands for each actuator, which facilitates parameter tuning on actuators and improves the convergence rate. These features enable the strategy to be suitable for large displacement loading and to exhibit a good tracking accuracy.
- The force-based loading strategy for redundant actuators can guarantee an optimal force distribution among multiple actuators. Compared with the displacement command correction approach, it does not require additional information on the specimen stiffness, and hence, is straightforward and easy to implement. A new performance index accompanies

this method, which simplifies the seeking process for optimal forces to the solving of linear simultaneous equations.

- Numerical simulations and verification tests validated the new loading strategy in terms of accuracy and ease of implementation. The application test showed the good performance and applicability of this strategy to large scale tests.

Acknowledgments

The authors gratefully acknowledge the financial support from the National Key Research and Development Program of China (Grant Nos. 2017YFC0703605 and 2016YFC0701106) and the National Natural Science Foundation of China (Grant Nos. 51878525 and 51778190).

References

Ahmadizadeh, M., Mosqueda, G. and Reinhorn, A. (2008), "Compensation of actuator delay and dynamics for real-time hybrid structural simulation", *Earthq. Eng. Struct. Dyn.*, **37**(1), 21-42. https://doi.org/10.1002/eqe.743

Bonnet, P.A., Lim, C.N., Williams, M.S., Blakeborough, A., Neild, S.A., Stoten, D.P. and Taylor, C.A. (2007), "Real-time hybrid experiments with newmark integration, mcsmd outer-loop control and multi-tasking strategies", *Earthq. Eng. Struct. Dyn.*, **36**(1), 119-141. https://doi.org/10.1002/eqe.628

Chae, Y., Ricles, J.M. and Sause, R. (2014), "Large-scale real-time hybrid simulation of a three-story steel frame building with magneto-rheological dampers", *Earthq. Eng. Struct. Dyn.*, **43**(13), 1915-1933. https://doi.org/10.1002/eqe.2429

Chang, C.M., Frankie, T.M., Spencer Jr, B.F. and Kuchma, D.A. (2015), "Multiple degrees of freedom positioning correction for hybrid simulation", *J. Earthq. Eng.*, **19**(2), 277-296. https://doi.org/10.1080/13632469.2014.962670

Chinese Standard GB. 50011-2010 (2016), Code for Seismic Design of Buildings, National Standard of the People's Republic of China (NSPRC); Beijing, China. [In Chinese]

Fermandois, G. and Spencer, B. (2017), "Model-based framework for multi-axial real-time hybrid simulation testing", *Earthq. Eng. Eng. Vib.*, **16**(4), 671-691. https://doi.org/10.1007/s11803-017-0407-8

Horiuchi, T., Inoue, M., Konno, T. and Namita, Y. (1999), "Real-time hybrid experimental system with actuator delay compensation and its application to a piping system with energy absorber", *Earthq. Eng. Struct. Dyn.*, **28**(10), 1121-1141. https://doi.org/10.1002/(SICI)1096-9845(199910)28:10<1121::AID-EQE858>3.0.CO;2-O

Iqbal, A., Pampanin, S. and Buchanan, A. (2008), "Experimental study of prestressed timber columns under bi-directional seismic loading", *Proceedings of New Zealand Society for Earthquake Engineering (NZSEE) Conference*, New Zealand. https://ir.canterbury.ac.nz/handle/10092/2658

Khoo, H.H., Tsai, K.C., Tsai, C.Y., Tsai, C.Y. and Wang, K.J. (2016), "Bidirectional substructure pseudo-dynamic tests and analysis of a full-scale two-story buckling-restrained braced frame", *Earthq. Eng. Struct. Dyn.*, **45**(7), 1085-1107. https://doi.org/10.1002/eqe.2696

Liu, G.Y. and Chang, S.Y. (2000), "Bi-axial pseudodynamic testing", *Proceedings of the 12th World Conference on Earthquake Engineering*, Auckland, New Zealand, January.

Liu, Y., Mei, Z., Wu, B., Bursi, O.S., Dai, K., Li, B. and Lu, Y. (2020), "Seismic behaviour and failure-mode-prediction method of a reinforced concrete rigid-frame bridge with thin-walled tall piers: Investigation by model-updating hybrid test", *Eng. Struct.*, **208**, 110302.

Mazzoni, S., McKenna, F., Scott, M.H. and Fenves, G.L. (2006), OpenSees command language manual, Pacific Earthquake Engineering Research (PEER) Center; University of California, Berkeley, CA, USA.

Mercan, O., Ricles, J.M., Sause, R. and Marullo, T. (2009), "Kinematic transformations for planar multi-directional pseudodynamic testing", *Earthq. Eng. Struct. Dyn.*, **38**(9), 1093-1119. https://doi.org/10.1002/eqe.886

Molina, F.J., Verzeletti, G., Magonette, G., Buchet, P.H. and Geradin, M. (1999), "Bi-directional pseudodynamic test of a full-size three-storey building", *Earthq. Eng. Struct. Dyn.*, **28**(12), 1541-1566. https://doi.org/10.1002/(SICI)1096-9845(199912)28:12<1541::AID-EQE880>3.0.CO;2-R

Nakashima, M., Takai, H. and Kenkyūjo, K.K. (1985), "Use of substructure techniques in pseudo dynamic testing", Research Paper No. 111; Building Research Institute of Japan, Ministry of Construction, Tsukuba, Japan.

Nakashima, M., Kato, H. and Takaoka, E. (1992), "Development of real-time pseudo dynamic testing", *Earthq. Eng. Struct. Dyn.*, **21**(1), 79-92. https://doi.org/10.1002/eqe.4290210106

Nakata, N., Spencer Jr, B.F. and Elnashai, A.S. (2010), "Sensitivity-based external calibration of multiaxial loading system", *J. Eng. Mech.*, **136**(2), 189-198. https://doi.org/10.1061/(ASCE)0733-9399(2010)136:2(189)

Nakata, N., Krug, E. and King, A. (2014), "Experimental implementation and verification of multi-degrees-of-freedom effective force testing", *Earthq. Eng. Struct. Dyn.*, **43**(3), 413-428. https://doi.org/10.1002/eqe.2351

Ou, G., Ozdagli, A.I., Dyke, S.J. and Wu, B. (2015), "Robust integrated actuator control: Experimental verification and real-time hybrid-simulation implementation", *Earthq. Eng. Struct. Dyn.*, **44**(3), 441-460. https://doi.org/10.1002/eqe.2479

Pan, P., Zhao, G., Lu, X. and Deng, K. (2014), "Force–displacement mixed control for collapse tests of multistory buildings using quasi-static loading systems", *Earthq. Eng. Struct. Dyn.*, **43**(2), 287-300. https://doi.org/10.1002/eqe.2344

Pan, P., Wang, T. and Nakashima, M. (2015), *Development Of Online Hybrid Testing: Theory And Applications To Structural Engineering*, Butterworth-Heinemann, Oxford, UK.

Phillips, B.M., Takada, S., Spencer Jr, B.F. and Fujino, Y. (2014), "Feedforward actuator controller development using the backward-difference method for real-time hybrid simulation", *Smart Struct. Syst., Int. J.*, **14**(6), 1081-1103. https://doi.org/10.12989/sss.2014.14.6.1081

Shao, X., Mueller, A. and Mohammed, B.A. (2016), "Real-time hybrid simulation with online model updating: Methodology and implementation", *J. Eng. Mech.*, **142**(2), 04015074. https://doi.org/10.1061/(ASCE)EM.1943-7889.0000987

Takanashi, K., Taniguchi, H. and Tanaka, H. (1980), "Inelastic response of H-shaped columns to two dimensional earthquake motions", Report NO. 13; Bulletin of Earthquake Resistant Structure Research Center. http://www.ers.iis.u-tokyo.ac.jp/PDF/ERSNo.13/1980-03-No.13-04.pdf

Tan, Q., Wu, B., Shi, P., Xu, G., Wang, Z., Sun, J. and Lehman, D.E. (2020), "Experimental performance of a full-scale spatial RC frame with buckling-restrained braces subjected to bidirectional loading", *J. Struct. Eng.* (Under review)

Tang, Z., Dietz, M., Li, Z. and Taylor, C. (2018), "The performance of delay compensation in real-time dynamic substructuring", *J. Vib. Control*, **24**(21), 5019-5029. https://doi.org/10.1177/1077546317740488

Thewalt, C.R. and Mahin, S.A. (1995), "Non-planar pseudo-dynamic testing", *Earthq. Eng. Struct. Dyn.*, **24**(5), 733-746.

https://doi.org/10.1002/eqe.4290240509

Tsai, K.C., Wang, H.Y., Chen, C.H., Liu, G.Y. and Wang, K.J. (2001), "Substructure pseudo dynamic performance of hybrid steel shear panels", *Steel Struct*., **1**, 95-103.

Wagg, D. and Stoten, D. (2001), "Substructuring of dynamical systems via the adaptive minimal control synthesis algorithm", *Earthq*. *Eng*. *Struct*. *Dyn*., **30**(6), 865-877. https://doi.org/10.1002/eqe.44

Wang, Z., Wu, B., Bursi, O.S., Xu, G. and Ding, Y. (2014), "An effective online delay estimation method based on a simplified physical system model for real-time hybrid simulation", *Smart Struct*. *Syst*., *Int*. *J*., **14**(6), 1247-1267. http://doi.org/10.12989/sss.2014.14.6.1247

Wang, J., Gui, Y., Zhu, F., Jin, F. and Zhou, M. (2016), "Real-time hybrid simulation of multi-story structures installed with tuned liquid damper", *Struct*. *Control Heal*. *Monit*., **23**(7), 1015-1031. https://doi.org/10.1002/stc.1822

Wang, Z., Wu, B., Xu, G. and Bursi, O.S. (2018), "An improved equivalent force control algorithm for hybrid seismic testing of nonlinear systems", *Struct*. *Control Heal*. *Monit*., **25**(2), e2076. https://doi.org/10.1002/stc.2076

Wang, Z., Ning, X., Xu, G., Zhou, H. and Wu, B. (2019a), "High performance compensation using an adaptive strategy for real-time hybrid simulation", *Mech*. *Syst*. *Signal Process*., **133**, 106262. https://doi.org/10.1016/j.ymssp.2019.106262

Wang, Z., Zhu, S., Xu, G., Xu, X. and Wu, B. (2019b), "Bi-directional hybrid test method and its verification", *J. Vib*. *Shock*, **38**(9), 1-8. [In Chinese] https://doi.org/10.13465/j.cnki.jvs.2019.09.001

Wu, T. and Song, W. (2019), "Real-time aerodynamics hybrid simulation: Wind-induced effects on a reduced-scale building equipped with full-scale dampers", *J. Wind Eng*. *Ind*. *Aerod*., **190**, 1-9. https://doi.org/10.1016/j.jweia.2019.04.005

Wu, B., Wang, Q., Benson Shing, P. and Ou, J. (2007), "Equivalent force control method for generalized real-time substructure testing with implicit integration", *Earthq*. *Eng*. *Struct*. *Dyn*., **36**(9), 1127-1149. https://doi.org/10.1002/eqe.674

Wu, B., Wang, Z. and Bursi, O.S. (2013), "Actuator dynamics compensation based on upper bound delay for real-time hybrid simulation", *Earthq*. *Eng*. *Struct*. *Dyn*., **42**(12), 1749-1765. https://doi.org/10.1002/eqe.2296

Wu, B., Tan, Q., Shi, P., Wang, Z., Xu, G., Sun, J. and Lehman, D.E. (2020), "Substructure modeling and loading control techniques for the test of a full-scale spatial RC frame with buckling-restrained braces subjected to bidirectional loading", *J. Struct*. *Eng*. (Under review)

Xu, G., Wang, Z., Wu, B., Bursi, O.S., Tan, X., Yang, Q., Wen, L. and Jiang, H. (2017), "Pseudodynamic tests with substructuring of a full-scale precast box-modularized structure made of reinforced concrete shear walls", *Struct*. *Des*. *Tall Spec*., **26**(16), e1354. https://doi.org/10.1002/tal.1354

Yang, G., Wu, B., Ou, G., Wang, Z. and Dyke, S. (2017), "Hytest: Platform for structural hybrid simulations with finite element model updating", *Adv*. *Eng*. *Soft*., **112**, 200-210. https://doi.org/10.1016/j.advengsoft.2017.05.007

Zhao, J., French, C., Shield, C. and Posbergh, T. (2003), "Considerations for the development of real-time dynamic testing using servo-hydraulic actuation", *Earthq*. *Eng*. *Struct*. *Dyn*., **32**(11), 1773-1794. https://doi.org/10.1002/eqe.301

Wang, Z., Xu, G., Li, Q. and Wu, B. (2020), "An adaptive delay compensation method based on a discrete system model for real-time hybrid simulation", *Smart Struct*. *Syst*., *Int*. *J*., **25**(5), 569-580. https://doi.org/10.12989/sss.2020.25.5.569

BS